Dynamic recrystallization and mechanical behavior of Mg alloy AZ31: Constraints from tensile tests with in-situ EBSD analysis

Gaetan Boissonneau, Andrea Tommasi, Fabrice Barou, Marco A. Lopez-Sanchez, Maurine Montagnat

To cite this version:

Gaetan Boissonneau, Andrea Tommasi, Fabrice Barou, Marco A. Lopez-Sanchez, Maurine Montagnat. Dynamic recrystallization and mechanical behavior of Mg alloy AZ31: Constraints from tensile tests with in-situ EBSD analysis. 2023. hal-04388880

HAL Id: hal-04388880
https://hal.science/hal-04388880

Preprint submitted on 15 Jan 2024

Dynamic recrystallization and mechanical behavior of Mg alloy AZ31: Constraints from tensile tests with in-situ EBSD analysis

Gaëtan Boissonneau[a], Andréa Tommasi[a], Fabrice Barou[a], Marco A. Lopez-Sanchez[b], Maurine Montagnat[c]

[a] *Geosciences Montpellier, CNRS, Université de Montpellier, France*
[b] *Departamento de Geología, Universidad de Oviedo, Spain*
[c] *Univ. Grenoble Alpes, CNRS, IRD, G-INP, IGE, Grenoble, France*

Abstract

We conducted tensile tests on AZ31 samples with in-situ SEM-EBSD acquisition at 250°C and 10^{-3} s^{-1} to study the evolution of dynamic recrystallization and its effect on the mechanical behavior. To investigate the entire deformation range up to failure at 65-67% engineering strain, stepwise experiments were conducted with in-situ EBSD acquisition at 2-5% strain intervals and repolishing of the samples at 15% strain intervals. All experiments show a consistent mechanical behavior characterized by a transition from hardening to quasi-steady state at $\sim$10% strain, followed by softening for strains greater than 35%. The bulk intragranular misorientation, quantified by the mean kernel average misorientation, increases steadily. Analysis of the EBSD maps shows that the quasi-steady state is associated with dominant dislocation reorganization (polygonization), whereas the onset of softening is linked to a net and continuous increase in the recrystallized fraction. In situ EBSD mapping documents the local discontinuous nature of continuous dynamic recrystallization: (1) nucleation of strain-free grains by bulging and subgrain rotation, (2) grain growth, (3) re-accumulation of dislocations substructures and formation of new nuclei. Analysis of the textures shows that dynamic recrystallization slows down rotation and strengthtening of the textures. The observed steady state and softening behaviors result therefore from both geometrical (texture-induced) and microstructural (dislocation-related) softening due to dynamic recrystallization.

Keywords: Dynamic recrystallization, softening, texture, hexagonal materials, anisotropy, nucleation processes

1. Introduction

Dynamic recrystallization (DRX) shapes the mechanical properties and texture of polycrystalline materials during deformation at high temperature. It produces bulk softening by a series of processes, which occur at grain and lower scales (cf. reviews by Sakai et al.; Humphreys et al. [1, 2]). Local grain-to-grain strain incompatibility results in stress concentrations, which lead to nucleation by grain boundary migration (bulging), development of low-angle boundaries by reorganization of the dislocations within a grain, or both. The newly formed grains then grow as function of the local gradients in dislocation density, and the energy and properties of grain boundaries. If grain growth is slower than nucleation, DRX decreases the average grain size. DRX also changes the texture evolution as the newly formed grains inherit different orientations from the parent grains and may thereby affect the mechanical behavior. However, the local nature and complex interactions between these processes hinder the establishment of clear relations describing the impact of DRX on the mean properties of a polycrystal despite more than five decades of research efforts.

Tests with quasi in-situ Electron Backscatter Diffraction (EBSD) monitoring of the microstructure evolution allow combining: (1) local observations of the physical processes involved in DRX, (2) quantitative analysis of the microstructure changes at the polycrystal scale, and (3) the evolution of the mechanical behavior with increasing strain. Here we present tensile tests on AZ31 magnesium alloy samples covering a large strain range, up to 67% engineering strain, for fixed strain and temperature conditions, selected to maximize DRX. In addition to the evident industrial interest for a better understanding of DRX in magnesium alloys [3], the hexagonal symmetry and strong viscoplastic anisotropy of magnesium result in local strain incompatibility and stress concentrations, which trigger DRX. AZ31 alloys are therefore an excellent analog material to study the impact of DRX in materials in which it is an essential process during high-temperature deformation, but for which experiments using in-situ EBSD monitoring are not possible, like ice [4, 5] or rocks [6, 7].

In the present study, we analyze the mechanical and bulk microstructural data (intragranular misorientation, grain size, and recrystallized fraction) for seven samples deformed to final engineering strains ranging from 32% to 67%. We document the different processes involved in DRX based on sequential misorientation maps. We then compare the observed texture evolution with predictions of viscoplastic self-consistent simulations to constrain how the microstructural and textural changes produced by DRX impact the mechanical behavior.

2. Methods

2.1. Starting material

Bone-shaped tensile samples (Supplementary Material Fig. S1) were cut from a cylindrical rod of commercially pure hot-extruded AZ31 magnesium alloy by electric discharge machining at 30-35° to the initial extrusion direction. This results in a strong initial texture characterized by a girdle of $< c >$ axes at 55-60° to the traction axis, which inhibits twinning during elongation. Before deformation, the samples were annealed at 400°C for 24 hours and polished with: #2400 and #4000 mesh grits, 6, 3, and 1 µm oil-based diamond suspensions and Oxide Polishing Suspension (OPS). Ultrasonic ethanol baths were used to clean the surface between the different polishing steps and before EBSD analysis.

2.2. In-situ tensile testing

Tensile tests were conducted inside the CamScan X500-FE CrystalProbe SEM-EBSD chamber using a NewTec Scientific MT1000 high temperature tensile rig. Samples were heated to 250°C (T/Tf = 0.58) and deformed at a constant velocity of 7 µm s^{-1} (10^{-3} s^{-1} in strain rate at 0% strain). The temperature is controlled using thermocouples located under the sample heads and in the center of the gauge section. Engineering strains are calculated based on a 7 mm initial length. Stress data are corrected for the reduction in section with increasing strain by assuming conservation of volume and uniform deformation of the sample.

The deformation was halted at engineering strain intervals varying between 2 to 5% for EBSD mapping. Interruption of deformation at elevated temperatures disturbs the macroscopic mechanical response of the specimens (cf.

section 3.1). Two strategies were used to minimize the perturbation: (i) halting deformation while holding the sample at 250°C, which results in stress relaxation during mapping, and (ii) rapidly cooling the sample to 150°C upon reaching the target strain and keeping it at 150°C during the EBSD acquisition, which produces a stress peak due to thermal contraction.

Out-of-plane deformation during the experiment reduces the indexing rate of EBSD maps, particularly around grain boundaries and triple junctions, where dynamic recrystallization processes are expected to occur. By adjusting the averaging parameter of the Kikuchi pattern acquisition, i.e. increasing the number of Kikuchi patterns acquired in each measurement, we were able to obtain high quality EBSD maps for up to 15% cumulated engineering strain without repolishing. To map recrystallization processes at larger strains, samples were repolished at 15% strain intervals. This strategy produces a continuous dataset up to engineering strains of 67%.

2.3. EBSD acquisition and post-processing

EBSD was acquired on a fixed small domain in the central part of the sample during each experiment. In addition, at the end of each experiment, post-mortem EBSD maps of larger area were acquired after repolishing the samples. The acquisition conditions, area and step sizes for all maps are summarized in Supplementary Material Table T1.

The open-source MTEX MATLAB toolbox v5.6.1 (https://github.com/mtex-toolbox/mtex) has been employed to treat and analyze the EBSD data. Measurements with a mean angular deviation higher than 1.3° were neglected. Grain boundaries were identified using a 7.5° misorientation threshold and smoothed (two iterations). Grains defined by less than four pixels were dropped out from the dataset. EBSD data was smoothed using a half-quadratic filter within each grain.

We imaged and quantified the evolution of the microstructure based on: (1) the intragranular misorientation, (2) the grain sizes, and (3) the recrystallized fraction. The intragranular misorientation produced by the accumulation of geometrically necessary dislocations (GND), was estimated based on: (1) the kernel average misorientation (KAM), which is the average value of the misorientation between a pixel and its neighbors, (2) the grain orientation spread (GOS), which is the mean deviation of the local orientations relative to the mean orientation of the grain, and (3) the misorientation (axis and intensity) to the mean orientation of the grain (Mis2mean). The first order KAM data was used if not specified otherwise. KAM and Mis2mean maps were used to document subgrain boundaries and subgrain structures within a grain, respectively. For comparing KAM data over the entire dataset, the higher resolution EBSD maps were down-sampled to match the coarser step size (2 μm). Grain sizes were quantified by the diameter of a circle with the same area as the grain (i.e. equivalent diameter).

In the present study, recrystallized grains are identified based on either the GOS, which is a scalar measure of the intragranular misorientation, or the grain size. The justification for these criteria is that DRX creates new grains with initially small sizes and very low dislocation densities. Both criteria have limitations. Using solely a GOS threshold has the limitation of including statically recrystallized grains produced by the pre-deformation annealing as well as grains poorly oriented for dislocation glide that deform slowly in the DRX population. For instance, the undeformed samples have recrystallized fractions determined using this criterium of >90%. Using a grain size threshold, this problem is avoided, but this criterium suffers from apparent 2D section problems. One could therefore conclude that the best choice is to use a joint threshold. However, analyzing the RX fraction defined based each of these criterium separately allows to highlight different aspects of the RX process. The GOS threshold allows to discriminate newly formed RX grains with low dislocation densities from those that have a dislocation substructure due to either nucleation by polygonization or deformation subsequent to RX. The grain size threshold includes nuclei formed by any processes but keeps no memory of fast-growing RX grains; it allows to probe the grain growth rate. The absolute values of the two thresholds are chosen empirically. We present results for a GOS threshold of 1° and an equivalent grain diameter of 20 μm, based on the analysis of the KAM maps and grain size distributions. Different grain size and GOS threshold values result in different recrystallized fractions but define similar evolution trends (see Supplementary Material Fig. S2).

3. Results

3.1. Bulk mechanical behavior

All experiments display a consistent mechanical behavior well illustrated by the true stress/engineering strain curves for the two samples deformed up to the highest strain (Fig. 1). Sample H (purple curve in Fig. 1) was deformed outside the SEM without interruption until failure to be used as a reference. The true stress/engineering strain curve displays an elastic loading phase of up to 2% strain, followed by a hardening stage up to 10% strain. From 10% to ∼30% strain, it exhibits a quasi-steady state behavior, which is followed by softening up to ductile failure at 63% strain. Optical inspection of the evolution of the sample shape with increasing strain did not document any progressive necking, but a catastrophic development of a semi-brittle shear band at the end of the experiment (see Supplementary Material Fig. S3).

The behavior of Sample X is representative of the mechanical response of the experiments in which the deformation was halted for in-situ EBSD mapping. Each interruption induced a stress relaxation, which is manifested as a vertical drop in the stress/strain curve. Three distinct deformation experiments (0% to 35%; 35% to 47%; 47% to 67%) were performed sequentially on this sample, with unloading and repolishing of the sample surface between the experiments. The true stress/engineering strain curves of the three experiments were assembled to construct the curve shown by the blue line in Fig. 1. The stress relaxation at 10% strain is a consequence of a reboot of the tensile rig software during the experiment due to a technical issue.

The two strategies for EBSD acquisition presented in section 2.3 have been tried on this sample: the segments of the curve displayed with full lines in Fig. 1 present data for EBSD acquisition at 150°C, whereas those displayed as dashed lines show the data for EBSD acquisition at 250°C. Despite the stress relaxation due to the interruption of the traction during the EBSD acquisition, the mechanical behavior of the samples with in-situ EBSD acquisition is consistent with that of sample H. It is characterized by elastic loading up to 2% strain, transition from hardening to quasi-steady state around 10% strain, and onset of softening around 35-37% strain. The stress peak at 35% strain for sample X is a consequence of thermal contraction of the sample as it was cooled down to room temperature. This might have caused some hardening and explain the 10 MPa offset of the mechanical data for strains

>35%. For the other experiments, unloading and cooling were synchronized to avoid such stress peaks. Post-mortem optical analysis of the sample at the end of the experiment highlights a stronger out-of-plane deformation and incipient necking in a ∼3 mm wide domain at the center of the specimen (see Supplementary Material Fig. S3). In the experiments halted at lower strains, necking is not observed.

3.2. Bulk microstructural evolution

The increase in KAM values show a steady accumulation of lattice misorientation (i.e., of GNDs) throughout the deformation experiment for all samples (Fig. 2.a). The median increases quasi-linearly, but the KAM distribution becomes progressive more skewed, due to faster increase of the higher values relative to the median, marking the development of low angle grain boundaries with progressively higher misorientations. Domains characterized by null KAMs are preserved over the entire deformation range. The data from the first experiment on Sample X show slightly higher rates of lattice misorientation accumulation than the remainder of the dataset. However, this difference may result from a sampling bias, as these data have been collected with a coarser step size than the remainder of the data (cf. Supplementary Material Table T1).

The grain size shows a two-step evolution (Fig. 2.b). All parameters describing the grain size distribution (median, first and third quartiles, and maximum excluding outliers) decrease with strain up to 35% engineering strain and remain almost constant afterwards. Median equivalent diameters evolve abruptly from >20 μm to ∼7 μm at strains >35%. Note, however, that this shift in behavior has not been observed within a continuous experiment, but between successive experiments. Moreover, due to the limited area of the domains analyzed during in-situ mapping, boundary grains could not be eliminated from the dataset, biasing the estimation of the equivalent diameters towards lower values.

The RX fraction, that is, the area fraction of the map occupied by recrystallized grains, defined using a 1° GOS threshold (see section 2.3) is initially very high because of artifacts (Fig. 3.a). Indeed, undeformed samples have "statically" recrystallized fractions ranging between 88-91%. As deformation proceeds, the recrystallized fraction drops quickly to low values (<5%)

as the annealed grains start to accumulate dislocations. Despite some variability among samples, due to the small mapped areas, the recrystallized fraction remains stable, below 5% up to 35% engineering strain. A sudden increase in the RX fraction is observed at ∼35% strain. In the 35% to 48% interval the RX fraction ranges between 7 and 12%. Thereafter, it fluctuates between 5 and 8%, but the last strain interval is documented by a single experiment. Post-mortem analysis of sample H documents higher RX fractions of 17% - 20% with the highest fractions measured in the vicinity of the localized shear band.

Defining recrystallized grains based on a 20 μm equivalent diameter threshold (Fig. 3.b) results in low RX fractions (<5%) up to 10% strain. Data for strains between 10% and 35% strain show a higher dispersion, but the RX fraction remains below 10%. Similarly to the RX fraction defined based on the GOS criterium, a sudden increase in the RX fraction is observed at 35% strain. Both samples deformed to higher strains display a steady increase in recrystallized fraction up to the end of the experiments, but the rates of increase differ between the two experiments. The maximum RX fraction, observed for sample F at 47% engineering strain, is of 28%.

3.3. Recrystallization processes

The evolution of the microstructure from the annealed state up to 12% strain is illustrated using KAM maps of sample X (Fig. 4). Before deformation, grains have smooth boundaries and sizes ranging between 30 to 100 μm. Due to the pre-deformation annealing, KAM values are mostly below 1°, thus most grains are identified as recrystallized based on the GOS criterium. A few grains preserved scarce subgrain boundaries. At 6% engineering strain, most grains display significant intragranular misorientations and the RX fraction based on the GOS is reduced to 15% (Fig. 3.a). Accumulation of dislocations and formation of subgrain boundaries is spatially heterogeneous, varying from grain to grain, but, in most cases, densities are stronger in the vicinity of grain boundaries (on average within <10 μm of the boundary). Apparent (2D) grain sizes hardly evolved, but grain boundaries became more serrated and local misorientations are intensified, leading to a decrease of the RX fraction defined based on the GOS to 3-4% at 12% engineering strain. At strains >10%, small grains (<10 μm) are observed locally, but these small grains do not always have GOS <1°. In summary, up to ∼10% engineering strain, the evolution of the substructure due to progressive accumulation of geometrically necessary dislocations is more pronounced than the changes in grain boundary geometry. This observation indicates that, under the present experimental conditions, dislocation mobility has faster kinetics than grain boundary mobility.

Analysis of the microstructure between 23% and 38% engineering strain for Sample D documents continuation of the same trend (Fig. 5.a). The more strained is the sample, the more serrated are the grain boundaries. The progressive increase in the misorientation across subgrain boundaries is well illustrated in the Mis2mean maps (right panel of Fig. 5.a). A zoom in the abnormally coarse grain that occupies most of the lower part of the map (Fig. 5.b) shows that the strong orientation gradient across the central part of the grain is accommodated by a network of low-angle boundaries, 10-20 μm wide. This network became more complex and misoriented with strain but did not evolve into a well-defined grain boundary. Most grains still have sizes in the 30 to 100 μm range, but small DRX grains are observed in all maps. The RX fraction based on GOS remains almost constant (Fig. 3.a), but that based on grain size slowly increases (Fig. 3b). The discrepancy between the two measures may be partially explained by the contribution of polygonization and subgrain rotation to DRX. This process is well illustrated by the DRX grain highlighted in green in Fig. 5.b, in which the new grain boundaries, formed by polygonization, enclose preexisting substructure. This process contrasts with nucleation by bulging, in which grain boundary migration cleans the dislocation substructure, producing DRX grains with little internal misorientation.

A marked switch in mechanical behavior, from quasi steady-state to softening (Fig. 1), accompanied by stabilization of the previously decreasing grain size (Fig. 2.b) and a sudden increase in the recrystallized fraction (Fig. 3) is observed around 35% engineering strain. The evolution of the microstructure after this transition is well illustrated by data for sample X between 35% and 47% engineering strain (Fig. 6). In situ EBSD data for the 47% to 65% strain interval provide similar observations. The grain size distribution is strongly bimodal with coarse grains (equivalent diameters $\geq$100 μm) and clusters of small DRX grains (equivalent diameters of 3-20 μm). Most DRX grains show little intracrystalline misorientation (GOS <1°). In the 35% to 65% strain interval, the DRX clusters show fast microstructural evolutions relative to the coarse grains. The RX fraction defined based on the grain size increases slowly by nucleation along the boundaries of the initial coarse grains, whereas that based on the GOS remains stable.

Relative to lower strains, which were dominated by polygonization, the contribution of nucleation and grain boundary migration to the evolution of the microstructure increases. Evidence of nucleation by bulging (grain boundary migration) with closure of the bulge by a subgrain boundary is widespread. This process is illustrated in Fig. 6.b, in which two grains formed by DRX are highlighted. The kinetics of the nucleation in the two cases is apparently distinct: the grain highlighted in purple formed progressively, whereas the one highlighted in green formed suddenly between 41% and 44% strain onto a previously slowly migrating boundary. The in-situ EBSD observations for this strain range highlight the discontinuous nature of the processes at the grain scale. The zoom in Fig. 6.c documents the evolution of a DRX grain, which was tracked based on its position and crystallographic orientation. This DRX grain grew fast at the expenses of its highly deformed neighbors, from 35% to 41% strain, while maintaining its intragranular structure almost free of dislocation substructures. At 44% growth slowed and dislocations started to accumulate, as documented by the build-up of substructures with misorientations that continued to increase up to 47% strain. This sequence also documents the formation of new DRX grains along the boundaries of this grain after 44% strain.

3.4. Texture evolution

The initial texture is characterized by a girdle of $< c >$ axes oblique to the tensile axis. We quantified the texture evolution by: (1) the change in the angle between the normal to the $< c >$-axis girdle and the tensile axis and (2) the intensity of the texture using a texture index proxy, the J-index (the integral of the squared orientation distribution function [8]). With increasing strain, the angle between the normal to the $< c >$-axis girdle and tensile axis, initially at 30-35°, decreases (Fig. 7.a). However, the texture reorientation rate progressively slows down and a quasi-steady orientation of the normal to the $< c >$-axis girdle at ∼20° to the tensile axis is attained after 35% engineering strain. The evolution of the orientation of the DRX grains (segmented based on the grain size) is, however, different. They initially display similar, but more dispersed, orientations than those of the parent grains, which control the bulk texture. However, after 35% strain, DRX grains have a texture characterized by a higher angle between the normal to the $< c >$-axis girdle and the tensile axis (ca. 24° at strains >45%).

The texture intensity does not vary significantly with increasing strain, with an almost constant bulk texture index around 4 for the datasets obtained on large areas at the start or after the experiments (Fig. 7.b). Higher texture indexes are estimated based on the smaller maps collected in-situ during the experiments, but these data are biased by the presence of a few coarse grains that occupy large area fractions of these maps (cf. Figs. 4 to 6). The DRX grains texture shows, like many other quantities in the present experiments, a change around 35% engineering strain. Up to 35% strain, it is slightly more dispersed than the bulk texture. Its dispersion then increases up to 40% strain and then it stabilizes at texture indexes between 2 and 2.5.

To quantify the effect of DRX on the texture evolution, we compare the measured textures to that predicted for uniaxial tension using a polycrystal plasticity model, in which deformation is solely accommodated by dislocation glide: the viscoplastic self-consistent model (VPSC [9, 10]). The simulation was performed using the VPSC7 code [11] with a 2^{nd} order linearization procedure, normalized critical resolved shear stresses (CRSS) for the basal $< a >$, prismatic $< a >$, and pyramidal $< a + c >$ systems of 1, 40, and 40 MPa with the EBSD maps from the annealed state of sample Y as a reference texture. The ratios between the CRSS of the different slip modes are derived from Zhang et al. (2021) [12]. Since the microstructural observations point to effective recovery, hardening is not implemented in these simulations. The initial texture is that measured for the starting material. VPSC models predict continuous concentration and reorientation of the texture, though at a progressively decreasing rate, towards parallelism between the normal to the $< c >$-axis girdle and tensile axis (continuous lines in Fig. 7). The texture evolution documented in the present experiments clearly deviates from the predictions of these DRX-free models. DRX produces therefore both dispersion and reorientation of the texture.

4. Discussion

4.1. Experimental limitations

The first limitation of the present study stems from the interruption of the deformation for in-situ acquisition of the EBSD data. Reducing the temperature produces thermal stresses in the sample, whereas keeping the sample at 250°C during the mapping may result in partial annealing and thus recovery. Then, the in-situ EBSD map sizes had to be kept small to prevent significant annealing and are therefore too small to be representative volume elements. To mitigate that, larger dimension maps were acquired post-mortem for most samples. These wide-ranging maps are used as reference to estimate the representability of the in-situ maps. The large number of EBSD maps acquired in the present study (61, cf. Supplementary Material Table T1) further ensures the statistical representability of the bulk microstructural parameters. For the mechanical response, the data from Sample H, deformed outside the SEM without interruption until failure, is used as a reference.

Due to the deterioration of the surface, acquisition of data on a single surface is limited to 15% cumulated strain before the samples had to be re-polished. However, the data presented in section 3.3 show that such a strain interval is sufficient to document the local DRX evolution. The analysis of multiple tests with overlapping strain intervals allows to verify the reproducibility of these observations and the sample scale evolution. Yet, the onset of widespread nucleation/growth around 35% was not observed within a single experiment, but by comparing different experiments. Finally, EBSD providing a two-dimensional description of the microstructure at the sample surface, growth of grain nucleus out of the observation plane cannot be discriminated from nucleation on the plane.

4.2. DRX processes

The present experiments document continuous DRX in AZ31. This process involves: (1) accumulation and reorganization of dislocations in low-angle boundaries networks, i.e., polygonization (Figs. 4 and 5) and (2) grain formation processes (Fig. 6), with nucleation by an association of bulging and subgrain rotation (Fig. 6.b) and growth of the RX grains by grain boundary migration (Fig. 6.c). In most cases, new RX grains initially show low dislocation densities, documenting the cleaning of the dislocation substructure by migrating boundaries (Fig. 6.c). However, as they grow, they re-accumulate dislocations and re-recrystallize (Fig. 6.c).

The DRX fraction remains limited up to 35% strain. Onset of widespread nucleation is associated with (1) a marked change in mechanical behavior, from quasi steady-state to softening (Fig. 1), (2) stabilization of the previously decreasing grain size (Fig. 2.b), and (3) sudden increase in the recrystallized fraction (Fig. 3). We infer that this rather long incubation period is needed to construct the dislocation substructure. Analysis of the KAM maps shows that substructure formation is more active during the hardening and steady-state phases of the experiments (Figs. 4 and 5) than during the softening phase (Fig. 6). The long incubation period suggests that, at the present experimental conditions, recovery may have delayed the onset of recrystallization. However, even when nucleation is dominated by bulging, the bulges are closed by subgrain boundaries that evolve into grain boundaries (Fig. 6.b), indicating that polygonization plays an important role in nucleation [5].

Comparison between the experimental textures and the texture evolution predicted by VPSC simulations highlights that during DRX both polygonization and nucleation/growth processes slow down the reorientation of the texture towards parallelism between the main Burgers vector, here $[\bar{1}2\bar{1}0]$, and the tensile direction (Fig. 7). The experimental textures show a constant orientation for all strains >35%, characterized by a bulk orientation of the normal to the $< c >$-axes girdle at ~20° to the tensile axis. RX grains are systematically more oblique to the tensile axis, having on average the normal to the $< c >$-axes girdle at ~24° to the tensile axis for all strains >45%. These observations suggest a stronger effect of nucleation/growth on the texture evolution.

The difference between the recrystallized fractions defined using the GOS or the grain size stems from the fact that the two thresholds focus on different aspects of the recrystallization process (Fig. 3). The GOS criterion only considers the intragranular dislocation density. Grains are identified as RX grains until they re-accumulate dislocations by deformation. The grain size criterium is more sensitive to grain growth. It also identifies as RX grains those formed by subgrain rotation, which may have dislocation structures inherited from the parent grains and hence GOS values >1°. This might explain the slightly higher RX fractions determined using the grain size criterium below 35% strain. However, the steady increase in the RX fraction after 35% strain determined using the grain size criterium while the RX fraction defined based on the GOS remains stationary results from slow grain growth relative to nucleation and build-up of dislocation substructures in the present experiments. This is corroborated by the marked grain size reduction (Fig. 2.b).

Nucleation/growth never spreads over the entire sample. It is localized, forming discontinuous network of small-grain clusters (Fig. 6.a). This suggests that nucleation is mainly controlled by plastic strain incompatibilities, relaxing local stress concentrations. The higher density of grain boundaries within the clusters may also favor further recrystallization within them, as it will favor the formation of dislocation pile-ups [13]. The RX fraction defined based on the grain size increases slowly as DRX progresses along the boundaries of the initial coarse grains linking the RX clusters. Progressive increase of the RX fraction and DRX spreading over large domains of the sample is consistent with the fact that necking only develops at high strains and quickly evolves into localized shear and failure.

4.3. Impact of DRX on the mechanical behavior

All samples show a consistent mechanical behavior characterized by a transition at ∼10% strain from hardening to a quasi-steady state, followed by softening for strains >35%. This contrasts with the steady increase of the KAM at the sample scale (Fig. 2.a). As the KAM directly correlates with the GND density, such an increase points to a steady increase in the GND content, which could lead to hardening. However, in the present experiments, polygonization may explain increase in KAM associated with a steady-state mechanical response. Organization of the dislocations into low angle boundaries and progressive increase of their misorientation by absorption of new dislocations allow for increase in the average KAM without decrease of the dislocation mean free path.

Onset of widespread nucleation and grain boundary migration controlled by contrasts in dislocation density are, however, required to explain the transition from steady-state to softening at strains >35%. These processes produce softening as the migrating grain boundaries clean the dislocation substructures (Fig. 6). They also increase the grain boundary area. This may have two opposite effects: (1) to enhance the contribution of grain boundary processes to deformation or (2) to hinder dislocation glide by increase in the density of high-angle grain boundaries, which will hinder dislocation glide and produce pile-ups, leading to hardening [14, 15]. In the present experiments, we observe both (1) a faster microstructural evolution of the DRX clusters relative to the remainder of the samples (Fig. 6.a) and (2) re-recrystallization of DRX grains (Fig. 6.c). These observations point to faster nucleation rates in the RX domains favored by stress concentrations due to dislocation pile-ups [13]. We hypothesize that fast re-recrystallization of DRX grains may avoid hardening by Hall-Petch processes during DRX.

DRX also produces softening by slowing down the texture evolution and therefore avoiding (or reducing) the geometrical hardening relative to that expected in absence of recrystallization. The relative contributions of the microstructural and the textural effects of DRX to the observed softening may be estimated by comparison between: (1) the mechanical behavior observed in the experiments, (2) the mechanical behavior predicted using the VPSC approach described in section 3.4, and (3) instantaneous tensional stresses predicted using the same VPSC model for the textures measured at different strains (Fig. 8). This comparison highlights that the geometrical weakening due to a slower texture evolution in the experiments alone could explain the quasi steady-state bulk mechanical behavior between 10 and 35% engineering strain, but cannot account for the bulk softening observed for strains >35%. The comparison also shows that the slower texture evolution in the experiments starts before evidence for widespread nucleation is observed. This suggests that polygonization may effectively slow down the texture evolution and produce thereby significantly bulk softening. VPSC predictions are dependent to the first order on the CRSS used for the different slip systems [9]. A less anisotropic single crystal behavior (lower contrast between the CRSS of the basal and prismatic and pyramidal systems) will result in slower texture evolution and weaker geometrical hardening without DRX, but qualitatively the results will be similar.

Although nucleation is localized, affecting relatively small volumes (RX area fractions <30%, Fig. 3.b) in the shape of spatially discontinuous clusters (Fig.6.a), it produces bulk softening of the sample by relaxation of local stress concentrations. Homogenization of the stresses within the sample by DRX could explain tensile deformation to high strains without necking. In contrast, the final deformation stages of sample H seem to indicate that development of a throughgoing recrystallization domain at the sample scale may result in strain localization, dramatic softening, and shear failure. The present data raise an additional question: What phenomenon does control the transition in macroscopic behavior between steady-state and softening: a critical RX fraction or a percolation threshold characterizing the continuity on a given scale (sample width) of the RX clusters?

5. Conclusion

All experiments show a consistent mechanical behavior characterized by transition at ∼10% strain from hardening to a quasi-steady state, followed by softening for strains >35%, despite a steady increase in the KAM (∼ geometrically necessary dislocation density) at the sample scale. Analysis of the EBSD maps shows that the quasi-steady state mechanical behavior is mainly associated with reorganization of the dislocations (polygonization), whereas the softening is linked to widespread nucleation and growth.
In-situ EBSD mapping allows monitoring the evolution of the dynamic recrystallization (DRX) process at both local and bulk (sample) scales. At the sample scale, the EBSD observations document a rather long incubation period up to 35% strain, which is dominated by dislocation accumulation and reorganization (polygonization), followed by widespread, but spatially heterogeneously distributed grain nucleation and growth. Closer analysis of the recrystallization (RX) clusters highlights the local discontinuous nature of DRX with nucleation by coupled bulging and subgrain rotation, grain growth and re-accumulation of dislocation substructures. At the studied experimental conditions, grain growth is slow relative to nucleation and build-up of dislocation substructures in the present experiments, producing a marked average grain size reduction. Despite the complexity and local nature of the DRX processes, the dataset acquired on multiple specimens is remarkably coherent.
In the present experiments, DRX grains are concentrated in clusters. DRX produces local softening and avoids stress concentrations due to strain incompatibility, since by cleaning the dislocation substructures and increasing the grain boundary area. Homogenization of the stresses within the sample by DRX could explain the observed tensile deformation to high strains without necking. DRX also slows down the texture strengthening compared to modeling, since the RX grains are preferentially oriented oblique to the tension direction, thereby decreasing the geometrical hardening relative to that expected in absence of recrystallization.

On a more technical note, the present results highlight the arbitrary nature of the criteria used for identifying RX grains and determining RX fractions. Use of grain orientation spread (GOS) and grain size threshold produce completely different results, even in a relative framework, as these criteria emphasize different aspects of the recrystallization process: decrease in the intragranular geometrically necessary dislocation density vs. grain size, which are controlled by the nucleation processes and the relative kinetics of nucleation, grain growth and re-accumulation of dislocation substructures.

Acknowledgements

This work was supported by the European Research Council (ERC) under the European Union Horizon 2020 Research and Innovation programme [grant agreement No 882450 – ERC RhEoVOLUTION]. We are grateful to Christophe Nevado from Géosciences Montpellier, for his support in the preparation of the EBSD samples. We thank Thomas Chauve for fruitful discussions. We also thank Juliette Grosset for help with final formatting of the paper.

References

[1] T. Sakai, A. Belyakov, R. Kaibyshev, H. Miura, J. J. Jonas, Dynamic and post-dynamic recrystallization under hot, cold and severe plastic deformation conditions, Progress in Materials Science 60 (2014) 130–207. doi:10.1016/j.pmatsci.2013.09.002.

[2] J. Humphreys, G. S. Rohrer, A. Rollett, Recrystallization and Related Annealing Phenomena, Newnes, 2017.

[3] T. Al-Samman, G. Gottstein, Dynamic recrystallization during high temperature deformation of magnesium, Materials Science and Engineering: A 490 (1-2) (2008) 411 – 420. doi:DOI: 10.1016/j.msea.2008.02.004.
URL `http://www.sciencedirect.com/science/article/B6TXD-4RTW3TJ-8/2/71432008df`

[4] M. Montagnat, T. Chauve, F. Barou, A. Tommasi, B. Beausir, C. Fressengeas, Analysis of Dynamic Recrystallization of Ice from EBSD Orientation Mapping, Frontiers in Earth Science 3 (2015).

[5] T. Chauve, M. Montagnat, F. Barou, K. Hidas, A. Tommasi, D. Mainprice, Investigation of nucleation processes during dynamic recrystallization of ice using cryo-EBSD, Philosophical Transactions of the Royal Society A: Mathematical, Physical and Engineering Sciences 375 (2086) (2017) 20150345. doi:10.1098/rsta.2015.0345.

[6] J. Urai, W. Means, G. Lister, Dynamic recrystallization of minerals, in: Mineral and Rock Deformation: Laboratory Studies, Geophysical Monograph, Hobbs, B.E. and Heard, H.C., 1986, pp. 161–200.

[7] M. A. Lopez-Sanchez, A. Tommasi, W. B. Ismail, F. Barou, Dynamic recrystallization by subgrain rotation in olivine revealed by electron backscatter diffraction, Tectonophysics (2021) 228916doi:https://doi.org/10.1016/j.tecto.2021.228916.
URL `https://www.sciencedirect.com/science/article/pii/S0040195121001980`

[8] H.-J. Bunge, J.-S. Lecomte, Texture Analysis in Materials Science H.-J. Bunge, Tech. rep. (1982). doi:10.13140/RG.2.1.1721.1041.

[9] R. A. Lebensohn, C. N. Tomé, A self-consistent viscoplastic model: prediction of rolling textures of anisotropic polycrystals, Mat. Sci. and Engin., A 175 (1993) 71–82.

[10] R. A. Lebensohn, M. I. Idiart, P. Ponte-Castañeda, P.-G. Vincent, Dilatational viscoplasticity of polycrystalline solids with intragranular cavities, Philosophical Magazine iFirst (2011) 1–30. doi:DOI: 10.1080/14786435.2011.561811.

[11] C. Tomé, R. Lebensohn, Manual for VPSC7c, Los Alamos National Laboratory, https://public.lanl.gov/lebenso/VPSC7c_manual.pdf (2012).

[12] F. Zhang, M. Sun, B. Sun, F. Zhang, Y. Bai, Z. Liu, Temperature Dependency on the Microscopic Mechanism in the Normal Direction of Wrought AZ31 Sheet under Dynamic Compressive Behavior, Materials 14 (23) (2021) 7436. doi:10.3390/ma14237436.

[13] P. Duval, F. Louchet, J. Weiss, M. Montagnat, On the role of long-range internal stresses on grain nucleation during dynamic discontinuous recrystallization, Materials Science and Engineering: A 546 (2012) 207–211. doi:10.1016/j.msea.2012.03.052.

[14] E. O. Hall, The Deformation and Ageing of Mild Steel: II Characteristics of the Lüders Deformation, Proceedings of the Physical Society. Section B 64 (9) (1951) 742. doi:10.1088/0370-1301/64/9/302.

[15] H. Adachi, H. Mizowaki, M. Hirata, D. Okai, H. Nakanishi, Measurement of Dislocation Density Change during Tensile Deformation in Coarse-Grained Aluminum by *In-Situ* XRD Technique with Tester Oscillation, Materials Transactions 62 (1) (2021) 62–68. doi:10.2320/matertrans.L-M2020861.

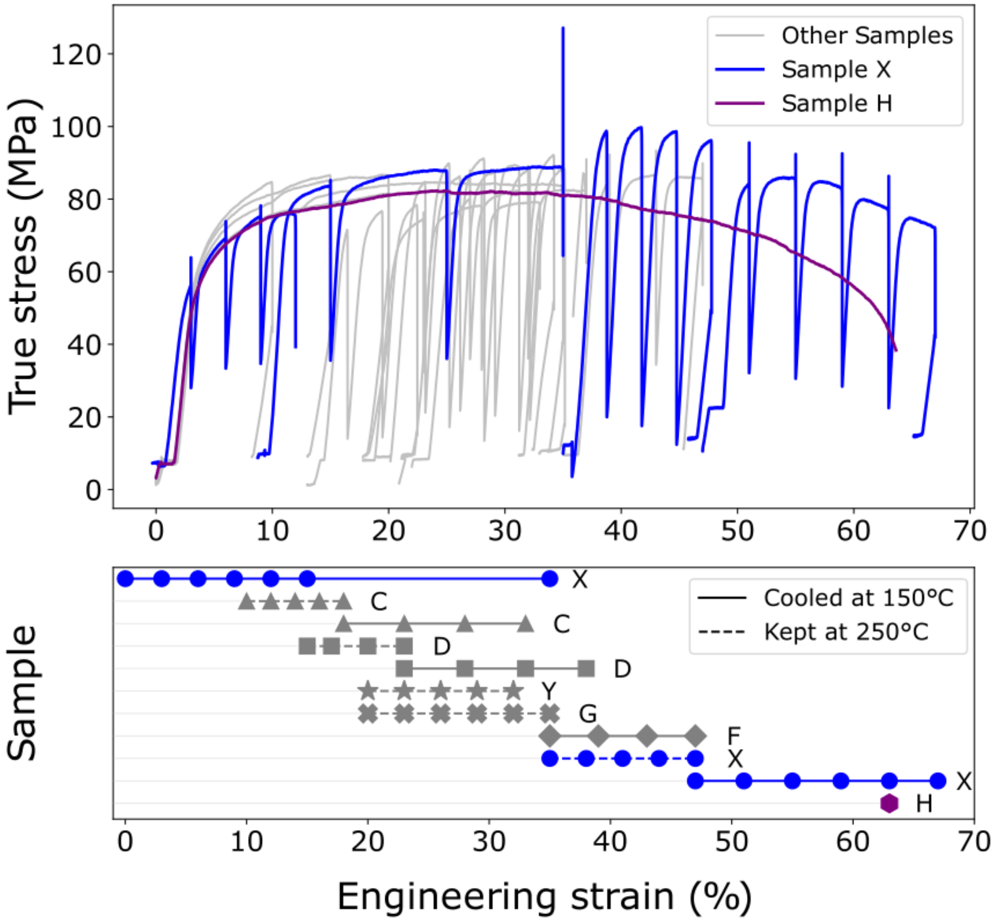

Figure 1: True stress/ engineering strain curves for all tests. Data for samples X and H, which cover the full strain range and are discussed in detail in the text, are highlighted in blue and purple, respectively. The lower panel details the experiments conducted on each sample: each line represents a continuous experiment with in-situ EBSD maps acquired without repolishing of the sample. Sample H was deformed without in-situ EBSD acquisition and is used as a reference.

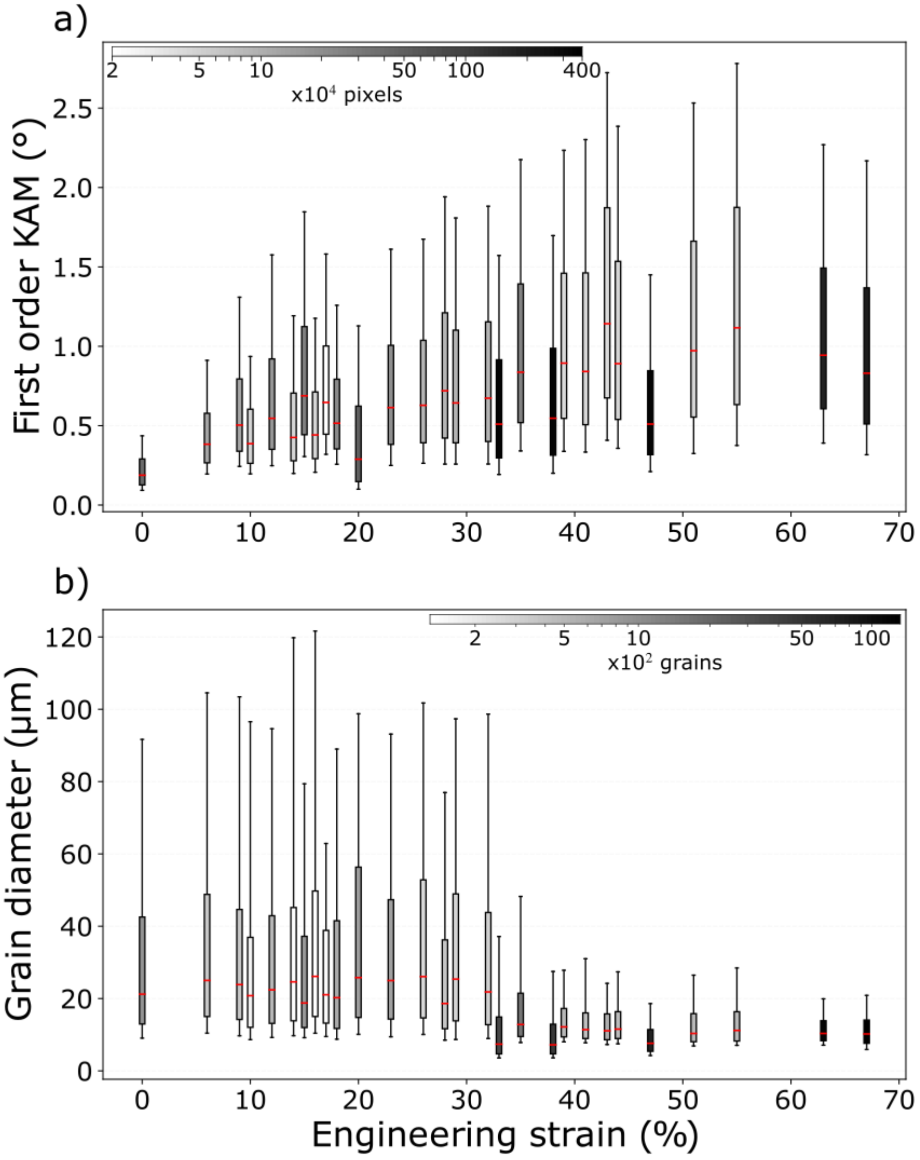

Figure 2: Evolution of the (a) intragranular misorientation and (b) grain size distributions with strain. Intragranular misorientation is defined by the 1st order Kernel Average Misorientation (KAM) and grain sizes, by the equivalent diameter. Data from multiple EBSD maps on a single or multiple samples at similar engineering strains were concatened to increase the statistics. The boxes define the first and third quartiles, the median is highlighted in red, and the extrem bounds of the whiskers represent the 10th and 90th percentiles of the data. The box color is function of the number of data points in each distribution, with darker colors marking the data with best statistics (graphic legends on the top of each plot).

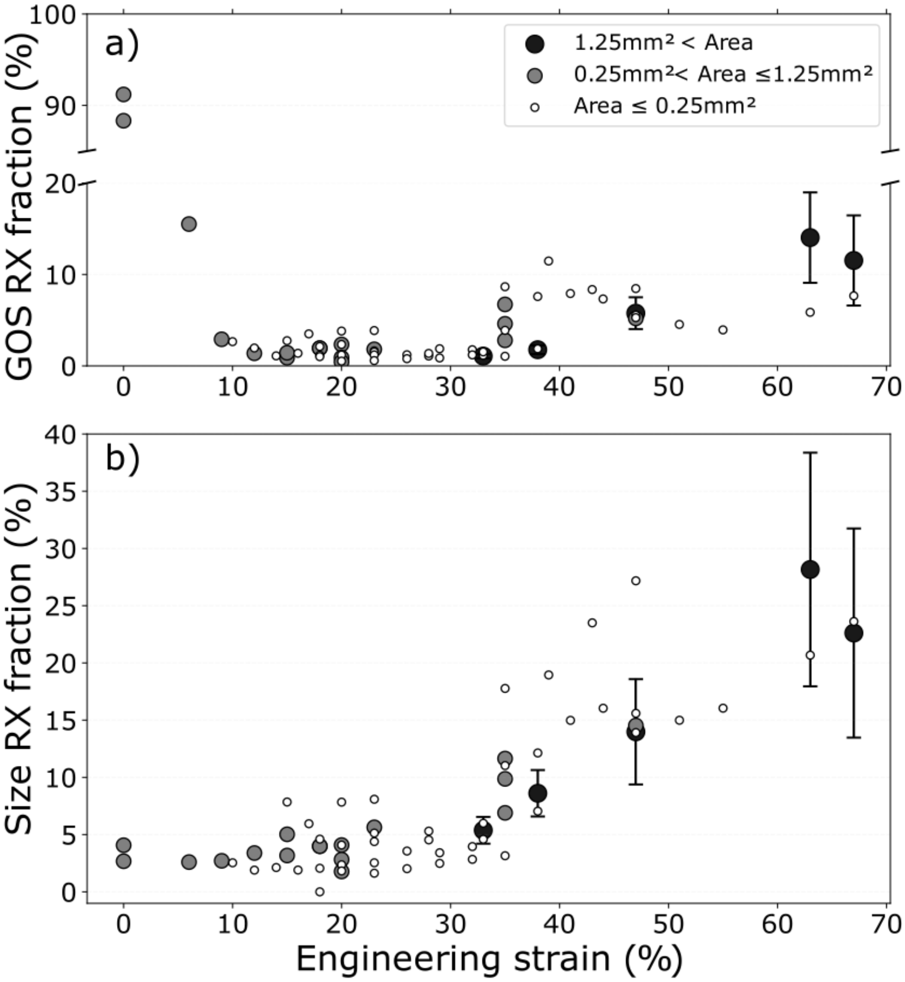

Figure 3: Evolution with strain of the recrystallized area fraction defined based on (a) a 1° GOS threshold and (b) a 20 μm equivalent diameter threshold. Symbol sizes indicate the total area of the EBSD map. To estimate the spatial variability of the data and the representativity of the smaller in-situ maps, the large maps (area > 1.25 mm^2) have been re-sampled as multiple smaller maps with areas similar to that of the in-situ ones (∼0,2 mm^2); this allows to estimate the mean and standard deviation, represented by the errorbars, of the recrystallized area fraction distribution in these maps.

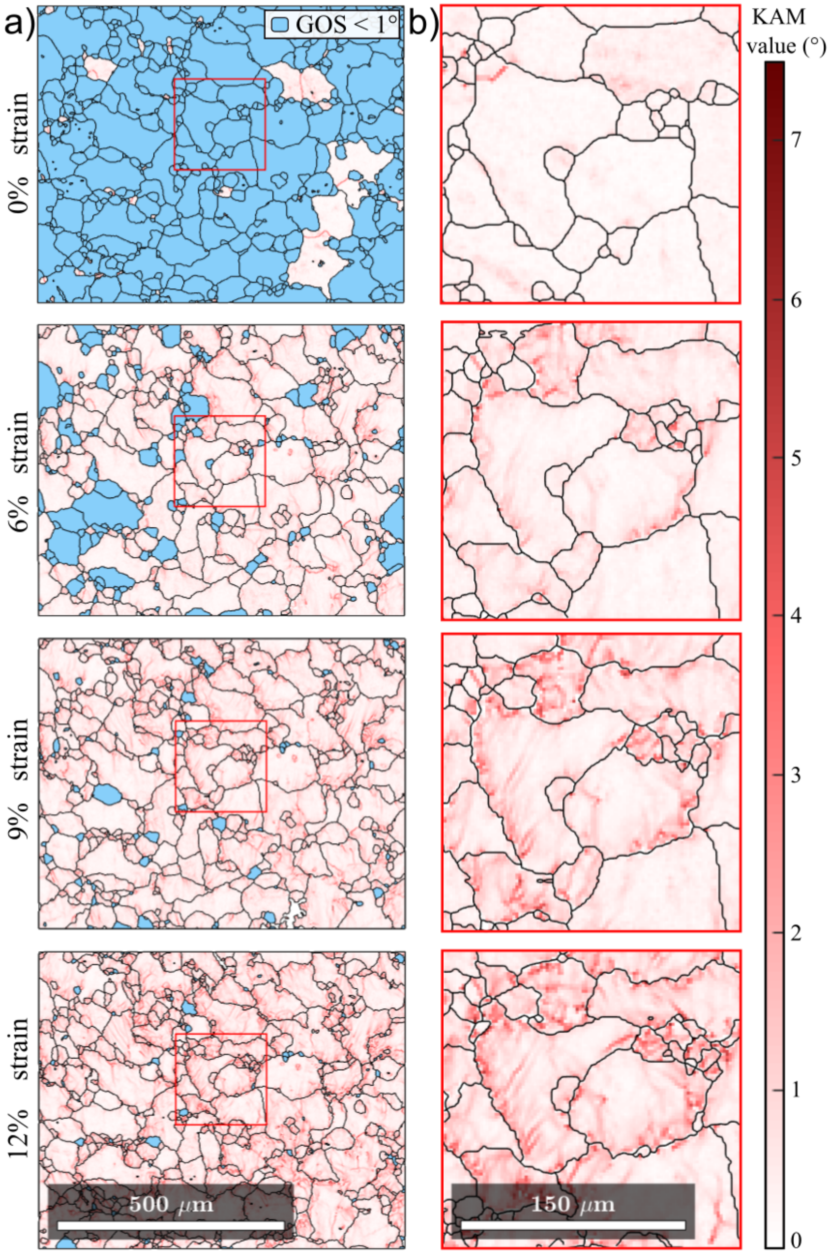

Figure 4: Microstructure evolution in the early stages of the experiments, illustrated by first order KAM maps obtained in situ at 0%, 6%, 9%, and 12% engineering strain for sample X. Grain boundaries, calculated using a 7.5° misorientation threshold, are represented as black lines. (a) Full size maps, in which the recrystallized grains identified using a 1°GOS threshold are coloured in blue. (b) Zoom on the area defined by the red square in (a); in these detail maps, KAM data for all grains are displayed, so that its evolution with strain may be followed.

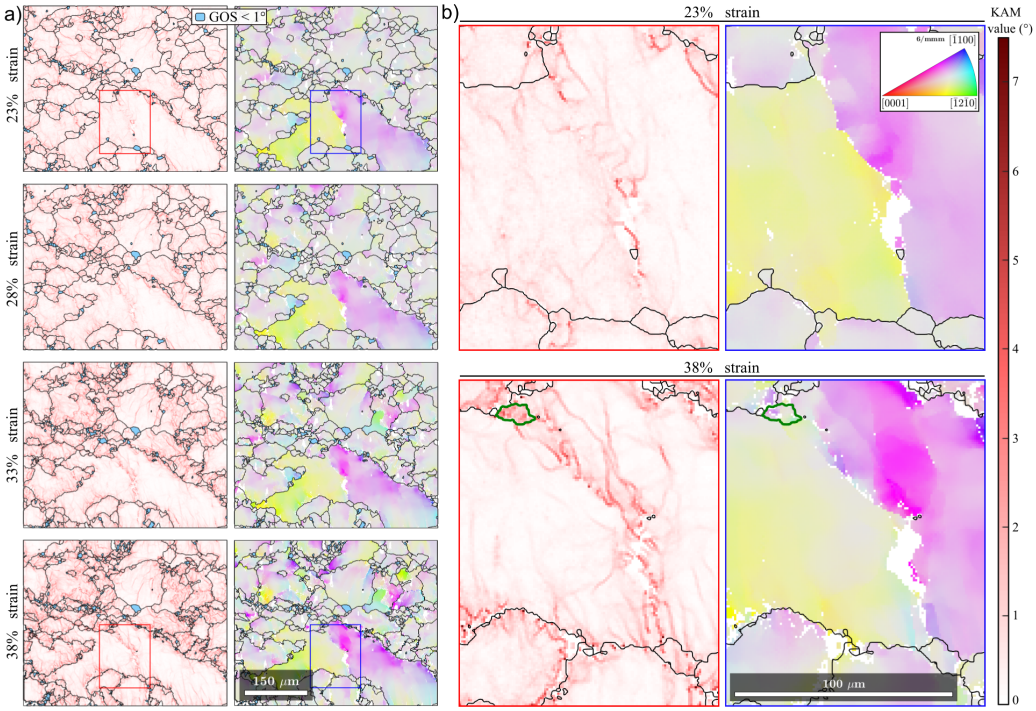

Figure 5: Microstructure evolution in the 23% to 38% strain interval, illustrated by in-situ first order KAM (left column) and mis2mean maps (right column) of sample D at 23%, 28%, 33%, and 38% engineering strain. Grain boundaries calculated using a 7.5° misorientation threshold are represented as black lines. (a) Full size maps, with recrystallized grains identified using a 1°GOS threshold coloured in blue. (b) Zoom on the area defined by the blue and the red rectangles in 23% and 38% engineering strain maps. A grain interpreted as formed by nucleation by subgrain rotation between 33% and 38% strain, is highlighted with a green boundary in the 38% strain detail maps, note its strong intragranular misorientation.

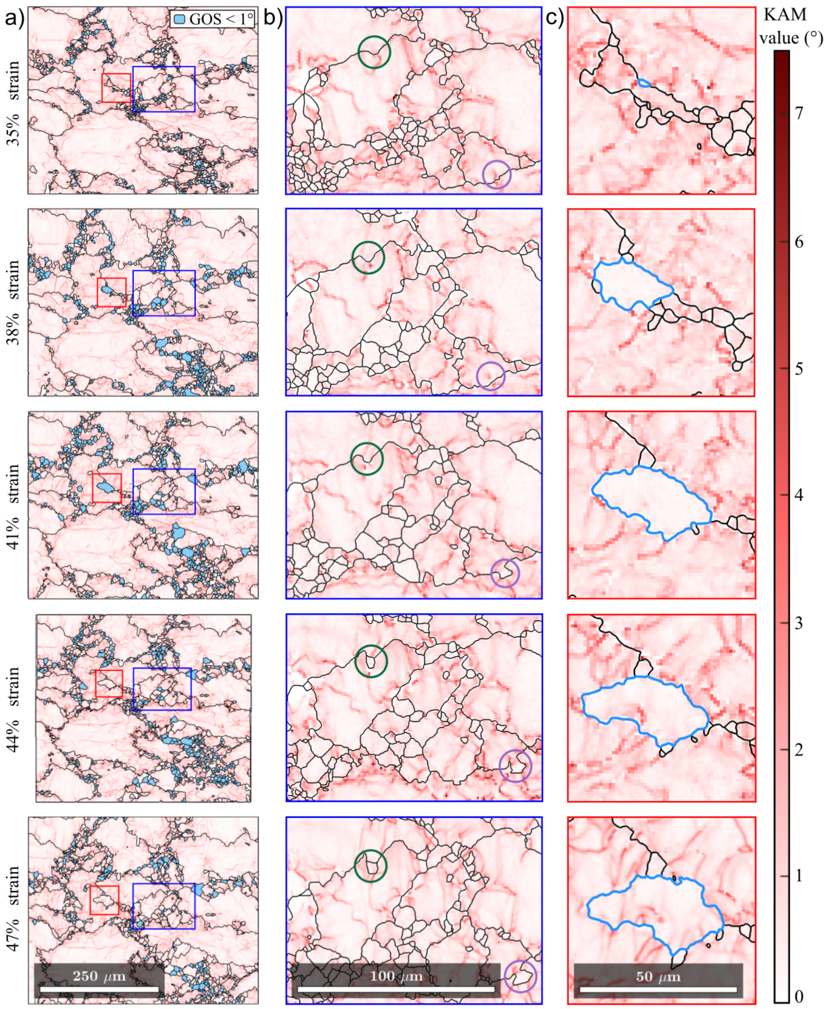

Figure 6: Microstructure evolution in the softening stage of the experiments, illustrated by KAM maps obtained in situ for sample X at 35%, 38%, 41%, 44%, and 47% engineering strain. All maps but that at 47% strain, were acquired with a 1 μm step size; the map at 47% strain was acquired with a step size of 0.5 μm. To keep absolute KAM values comparable over the entire strain range, the KAM order has been adjusted: first order KAM data is presented for all maps except for that at 47% strain strain, which displays second order KAM data. Grain boundaries calculated using a 7,5° misorientation threshold are represented by black lines. (a) Full size maps, in which recrystallized grains identified using a 1°GOS threshold are coloured in blue. (b) Zoom on the area defined by the blue rectangle in (a); dark green and purple circles are used to highlight areas showing nucleation events. (c) Zoom on the area defined by the red rectangle in (a), which displays the growth and re-accumulation of local misorientation in a recrystallized grain (highlighted in light blue) that is tracked using its location and crystallographic orientation from map to map.

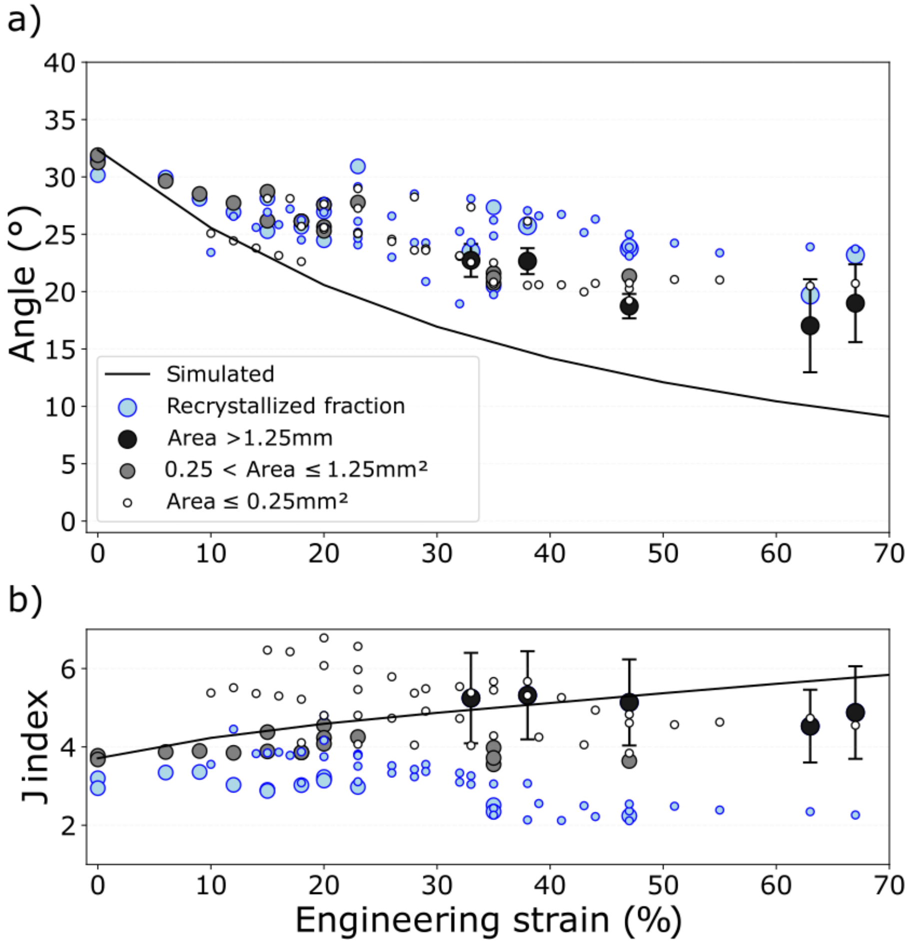

Figure 7: Evolution of the texture with engineering strain: (a) orientation of the texture, defined by the angle between the normal to the <c> axis girdle and the traction direction and (b) texture strength, defined by the J-index. Symbols in white, gray, and black correspond to full orientation data in the map, considered as one orientation per pixel. Coarser black symbols mark data from larger, post-mortem maps. To estimate the spatial variability of the data and the representativity of the smaller in-situ maps, these large maps (area > 1.25 mm^2) have been re-sampled as multiple smaller maps with areas similar to that of the in-situ ones (∼0.2 mm^2) to obtain the mean and the standard deviation, represented by the errorbars, of the distributions. For comparison, the texture of the recrystallized fraction identified using a 20 μm threshold in each map is represented by blue symbols; as for the full orientation data, the symbol sizes are proportional to the area of the map. The full lines indicate the texture evolution predicted by a 2^{nd} order viscoplastic self-consistent simulation for uniaxial traction with normalized critical resolved shear stresses (CRSS) for the basal<a>, prismatic<a>, and pyramidal<a+c> systems of 1, 40, and 40 MPa and as the initial texture that of the starting material.

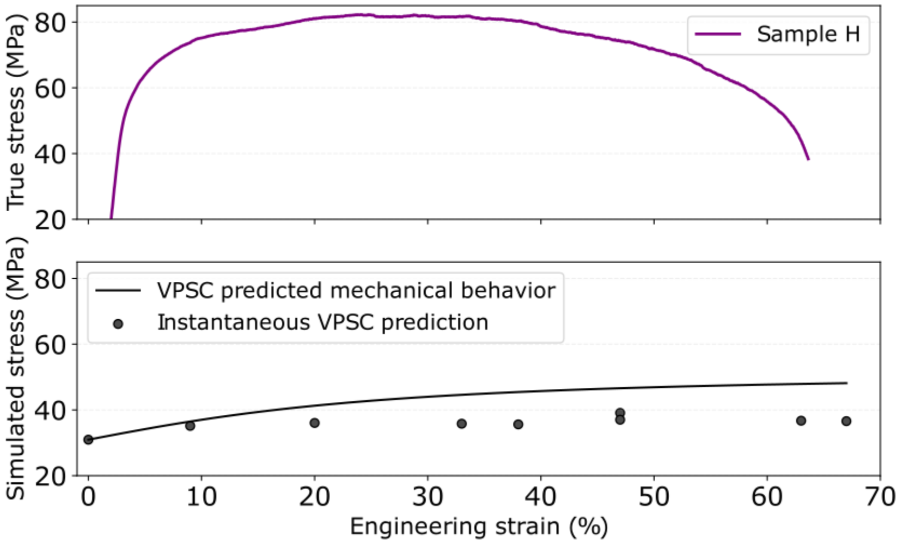

Figure 8: Comparison between the (a) mechanical behavior of Sample H, which was deformed without interruptions and (b) that predicted by a 2$^{\mathrm{nd}}$ order viscoplastic self-consistent simulation for a monotonic uniaxial traction experiment with normalized critical resolved shear stresses (CRSS) for the basal<a>, prismatic<a>, and pyramidal<a+c> systems of 1, 40, and 40 MPa and the initial texture of sample Y and the instantaneous tensional stresses predicted using the same VPSC model for textures measured at different engineering strains.